Chapter 3

Fabrication and Characterization Techniques

The methodology required to accomplish the set targets in the experimental research requires pertinent fabrication, characterization, and analytical tools and methods. Several factors must be considered before the selection of any techniques such as cost, time, availability, suitable environment, and performance. The fabrication, characterization, and analytical techniques all together are critically needed for in-depth study and proper understanding of device performance and related physics behind it. Moreover, after the material, film, and electrical characterization of films and devices, the parameter extraction out of the raw data is crucial to conclude mechanism. This chapter provides a brief explanation of various fabrication, characterization, and data extraction techniques used in this thesis.

3.1 ATOMIC LAYER DEPOSITION

Atomic layer deposition (ALD) belongs to the class of chemical vapor deposition (CVD) where atomically thin films of various materials such as oxide, nitrides, sulfides, metals, and fluorides can be deposited with proper stoichiometric control. Also, the films can be doped, can be grown in nano-laminate, and in nano-structure forms using ALD. ALD is known for producing highly conformal films on high aspect-ratio structures, uniform and precise thickness control, tunable stoichiometry, and films with fewer defects.

The deposition process involves self-limiting reactions of precursor molecules when the

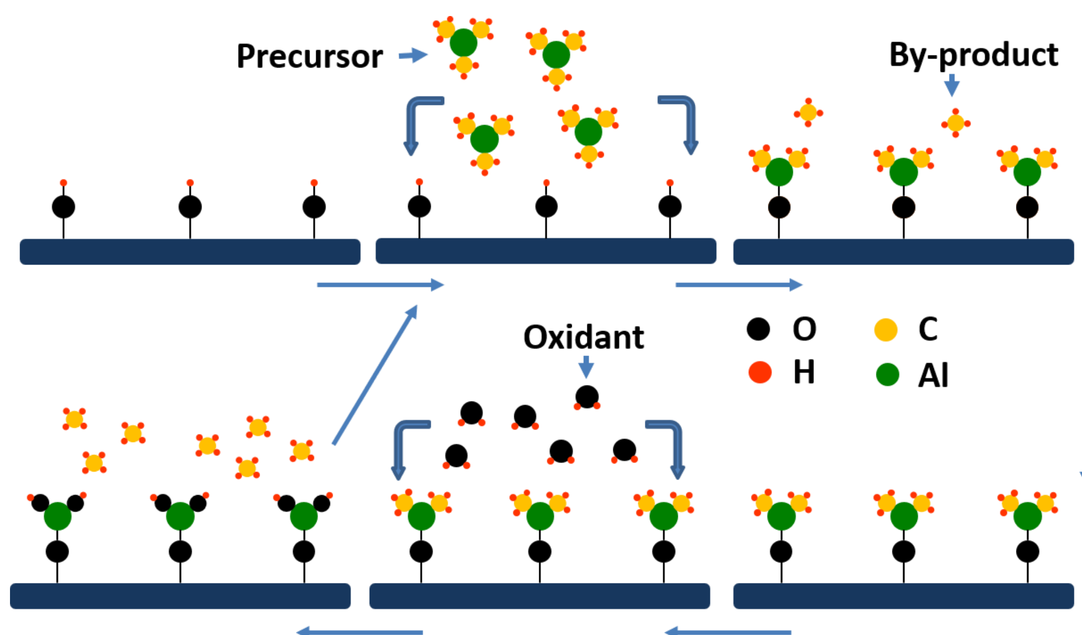

Figure 3.1: (a) Schematic diagram shows one complete cycle of atomic layer deposition.

inert carrier gas transports them into the reaction chamber through the alternating pulses designed for the desired process of precursors [Cremers *et al.*, 2019; George, 2010]. During the first half cycle, the first precursor vapors will be pulsed into the chamber for a concise period, where it reacts with the substrate surface and forms a monolayer. Sufficient time has been provided to the precursor to react with the substrate surface, and simultaneously, the by-products are pumped out of the chamber through purge gases. The second half-cycles involve the pulse and purging of the second precursor that reacts with the first one to form the monolayer of the desired material. To achieve the desired thickness, this process is cycled again and again in the vacuum chamber (<1 Torr), as shown in Figure 3.1. This thesis research has been performed on Savannah S200 ALD system from Cambridge Nanotech, as shown in Figure 3.2(a). In this research, the high-k dielectrics such as

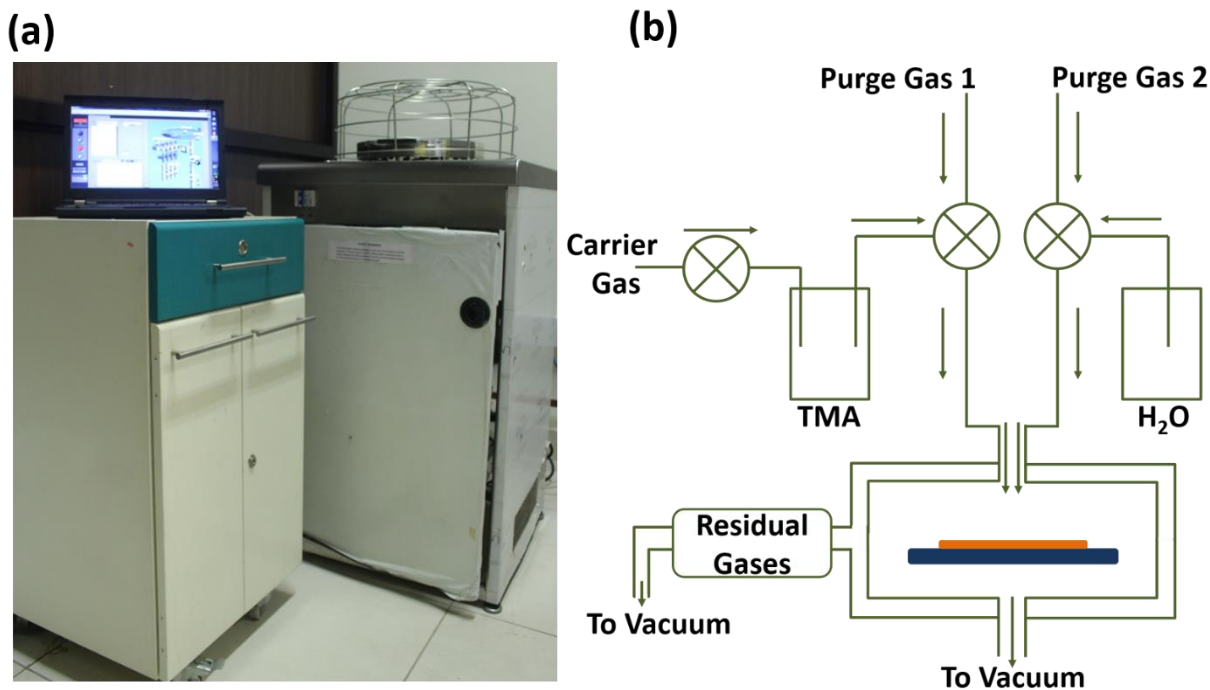

Figure 3.2: **(a)** Savannah S-200 ALD system from Cambridge nanotech used for research. **(b)** Schematic demonstrating the design of a process flow of ALD.

AlO_x using Trimethyl Aluminum (TMA) and H_2O and HfO_x using Tetrakis-dimethyl-amidohafnium (TDMAH) and H_2O as the precursors were deposited on rigid and flexible substrates. The system is capable of deposition of films at up to 300 ℃; however, this study involves the flexible substrates with lesser temperature tolerance; hence the maximum deposition temperature was kept at 100℃. Figure 3.2(b) displays the machine schematic demonstrating AlO_x deposition using TMA and H_2O.

3.2 SPIN COATING

The spin coating is the most common and widely used technique solution processible thin film deposition on a variety of substrates. The material we want to coat is mixed with a volatile solvent, stir or ultrasonicate them, and then the solution is spin-coated on the substrate at various rotation per minute (rpm) (1500 to 7000 rpm) to achieve the desired thickness [Birnie, 2004]. The combined effect of centripetal force and the surface tension of the solution while substrate rotation at high speed, results in the solution covering the complete substrate and. Later, the solution is annealed or left as it is for complete evaporation of the solvent. The film thickness also depends upon the solution viscosity, solvent evaporation rate, material density in the solution, duration of rotation, rotation acceleration, and sample position [Hall *et al.*, 1998]. The primary advantages of the spin coating technique are a simple setup, easy to use, low maintenance,

relatively cheaper, and faster way to produce uniform and thin films. On the contrary, spin coating is a batch process technique and hence low throughput. Also, the drying time of film is quite less that causes issues in producing self-assembly or crystalline coatings [Lawrence, 1988]. Moreover, the total material consumed for deposition is very low (~10%) and rest gets spill off the side and wasted [Ossila, 2016]. The spin coating method has been used in this research for deposition of PVP and its composites with GO and MoS_2. The spin- coating system we used for

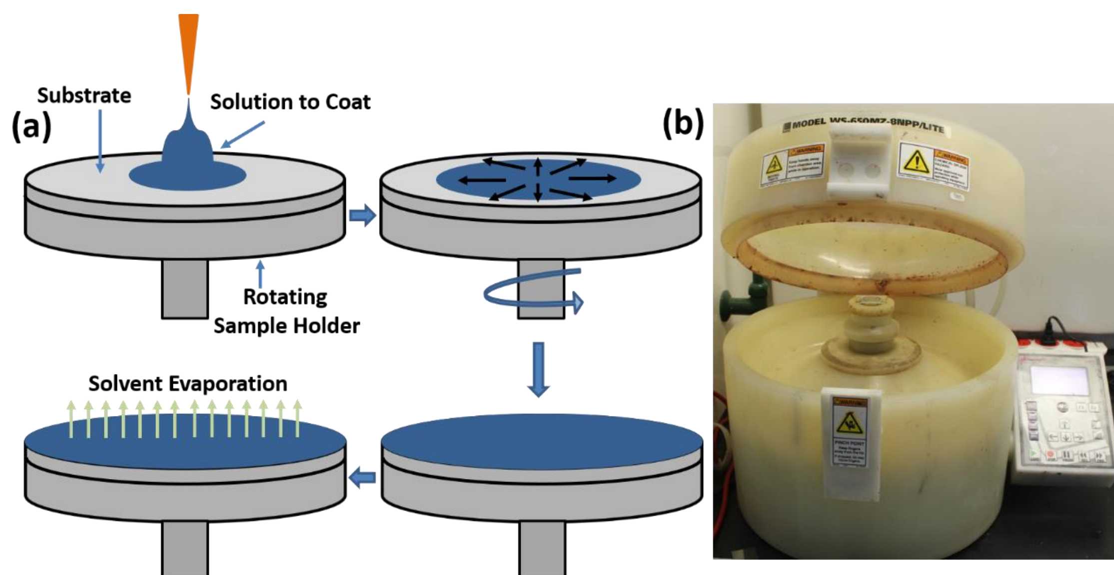

Figure 3.3: (a) Schematic demonstration of spin coating process. **(b)** WS-650 MHz-BNPP/LITE spin coating system from Laurell used in experiments.

this research is the WS-650 MHz-BNPP/LITE from Laurell. The deposition speed is varied from 4000 to 7000 rpm while the rotation time is kept between 45 to 60 s. After the deposition, the samples were left overnight for complete solvent evaporation. In some cases, the samples were annealed at 60 °C for 60 min. Figure 3.3(a) and (b) shows the deposition process using a schematic and the digital image of the spin coater system, respectively.

3.3 PHYSICAL VAPOR DEPOSITION

The physical vapor deposition technique involves the deposition of thin films with thickness ranging from nanometers to several micrometers. The target material in the vapor form is transferred to the substrate at an atomic level. This technique can be broadly classified into DC and RF sputtering, thermal evaporation, e-beam evaporation, and cathodic arc deposition [Mattox, 2010a]. The two main techniques used for this research are thermal and e-beam evaporation; hence, they will be explained in detail here. The deposition process involves four major steps:

i) Evaporation
ii) Transportation
iii) Reaction
iv) Deposition

During the evaporation stage, the target material is melted using the heating sources such as resistive boat or electron-bean hitting the target. The heating will turn the target into vapor for that will start dislodging atom by atom from the target surface. The transport process will carry the evaporated atom in a straight line, towards the substrate under high vacuum conditions (10^{-6} – 10^{-7} torr) [Sproul, 1996]. The deposition may include coatings of the metal oxides, nitrides, carbides, and other complex materials. In that case, the target will be the metal and it will react with the gas used during the transportation phase [Jurczyk, 2018]. The deposition phase includes

the formation of films at the substrate surface. The deposition chamber must be free from any contaminant gases or impurities otherwise issues such the film purity, desired film properties, and irregular film growth may arise that may hamper the purpose [Mattox, 2010b]. Figure 3.4(a) displays the schematic diagram demonstrating the physical vapor deposition process in a thermal/e-beam evaporation system. This research compiles the deposition of Ag thin films using the thermal evaporation system and Ti thin films using e-beam evaporation system SC-Triaxis from SemiCore. The digital image of SC-Triaxis-e-beam and thermal evaporation system is shown in Figure 3.4(b). The deposition Ag and Ti thin films were performed under high vacuum conditions of 10^{-6} torr at deposition rate of 1 ˚A/s. The Ag target material was kept in a tungsten boat whereas the Ti was kept in a quartz crucible to deposit 150-200 nm thick Ag and 200 nm thick Ti films.

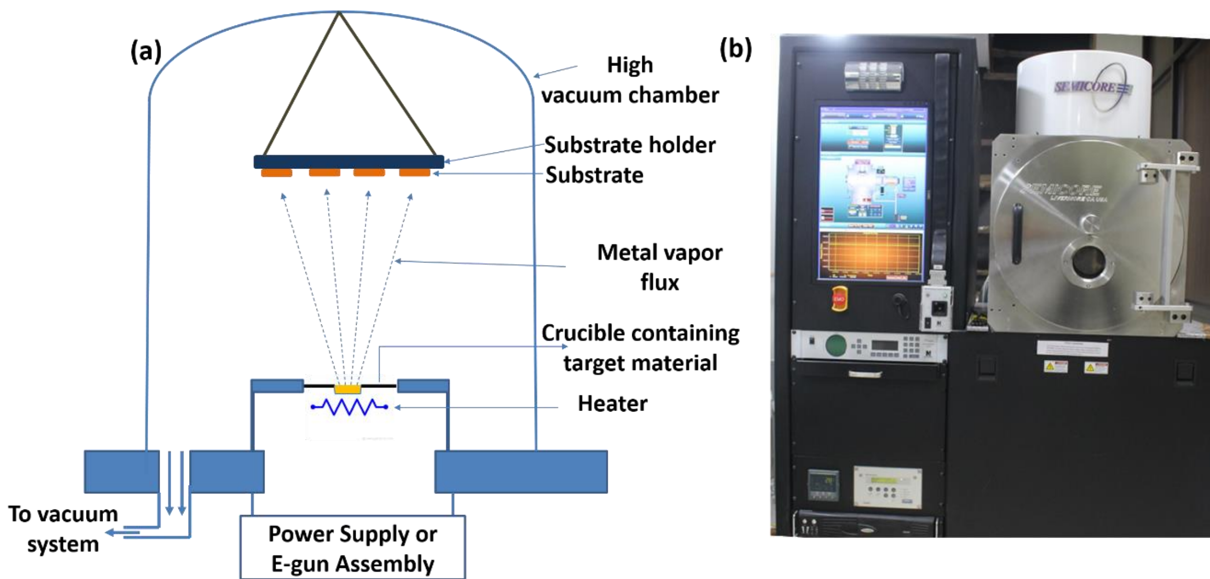

Figure 3.4: (a) Schematic demonstration of thermal/e-beam evaporation process. **(b)** SC-Triaxis physical vapor deposition system from Semicore used for this research.

3.4 SURFACE PROFILING

Surface profiling is one most popular and easy technique used to create profile and 2-D and 3-D images of the surface. Surface profiling of film is performed using a cantilever stylus based sharp probe that moves along the surface to sense the surface height, roughness, strain, stress, and many other properties. All these parameters are calculated using a feedback loop that measures the force exerted by the sample on the probe as it moves over the surface. The feedback system keeps the stylus force constant against the reaction received from the sample surface [Whitehead *et al.*, 1999]. These measurements are performed in contact mode operation with manually setting the stylus force and scan area. Due to the feedback system and the probe's movement in contact with surface, high sensitivity and high Z resolution can be achieved [Sheppard and Matthews, 1988]. Figure 3.5(a) explains the process involved in surface scan, data acquisition, and feedback controls. The contact mode operation makes this technique sensitive to the soft surface, as it may be a destructive approach. Moreover, the chance of probe contamination is also higher and frequent cleaning or changing the probe tip may lead to calibration issues, blur images, and inaccurate data extraction. Furthermore, this is a slower process than the non-contact operation as the contact force may drag the stylus movement. This research involves the usage of DektakXT Surface Profiler from Bruker shown in Figure 3.5(b), whose stylus radius is 2 µm, and scanned in Hills and Valley Mode.

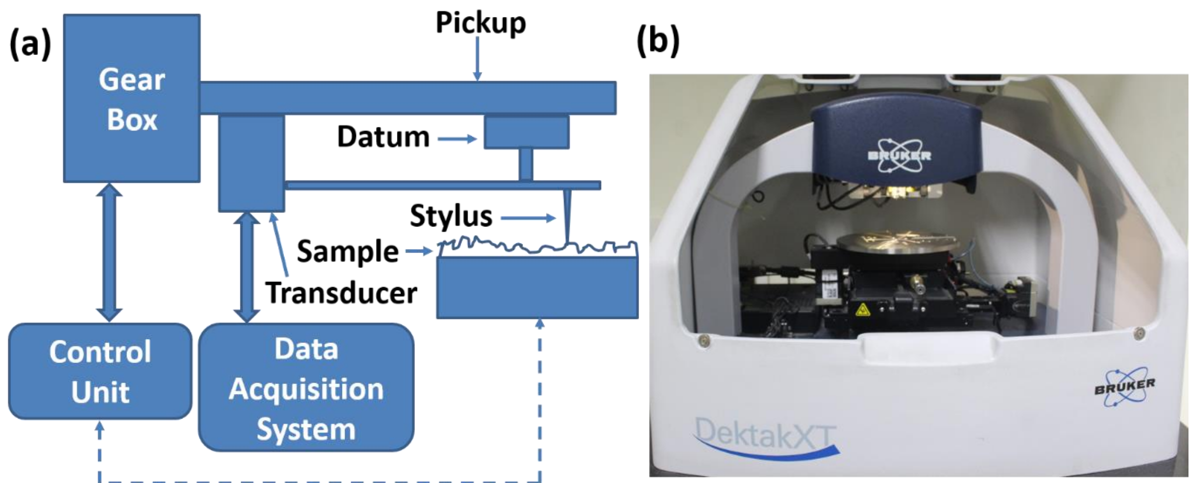

Figure 3.5: **(a)** Schematic diagram of surface profiler scanning the line profile using the stylus. **(b)** Digital image of DektakXT surface profilo-meter system from Bruker.

3.5 ATOMIC FORCE MICROSCOPY

After the invention of the atomic force microscope (AFM) by Binning, Quate, and Gerber in 1985, the AFM has become the most popular and advanced technique for surface scanning at the nano-scale that provides high resolution and three-dimensional images [Binnig *et al.*, 1986]. This technique has the advantage of scanning a broad category of surfaces that includes ceramics, glass, biological samples, and polymers. The major components that constitute an AFM are probes, optical detection system, piezo-scanners, and the electronics for The AFM scan is performed using a cantilever with a sharp tip with diameter 10-20 nm moving in raster-scan pattern to scan the selected area [Haugstad, 2012]. As the tip tends to move towards the sample surface, the cantilever bends upwards due to the ionic repulsive forces between the surface and the tip. The magnitude of this force may vary from 10^{-11} to 10^{-6} N. This force can be calculated using the amount of cantilever bends that have been measured using the laser spot reflection on to the

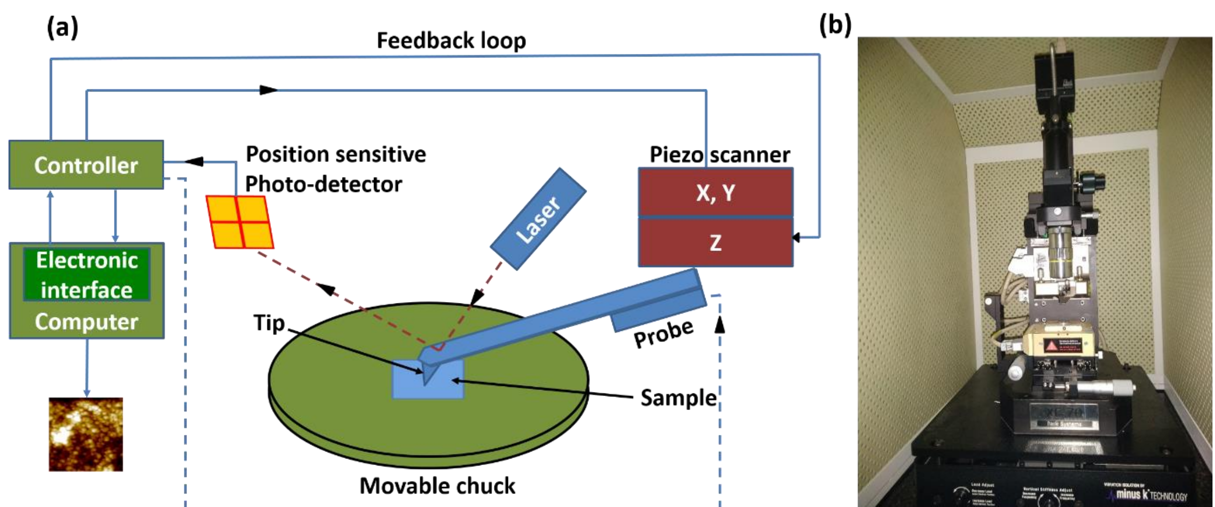

Figure 3.6: **(a)** Working principle explanation of the AFM. **(b)** Digital image of the XE-70 AFM from Park Systems used in this research.

position-sensitive photo-detector (PSPD) [Daniel Rugar, 1990]. The distance between the tip and the surface, known as the setpoint, is maintained constant using a feedback loop. The upwards deflection of as low as 0.1 A° in the cantilever can be measured by the PSPD. The surface

topography is recorded as the tip's vertical movement corresponds to the surface profile while keeping the tip force constant during the surface scan. In this research, the Park System's SPM XE-70 tool was used to perform the surface scanning in non-contact/tapping mode of operation. The working principle of AFM scanning and imaging technique and a digital image of the system has been shown in Figure 3.6(a) and (b), respectively.

3.6 SCANNING ELECTRON MICROSCOPY

The scanning electron microscopy (SEM) is one the most popular and widely accepted technique for surface morphology analysis at the nano-scale level. The SEM working principle states that when an incident electron beam from the filament interact/hit with the sample atoms, many signals will be generated where every signal carries some significant information. The SEM systems have the capability of producing images with magnification as high as 30,000× and resolution as low as 1 nm [Egerton, 2005; Reimer, 2000]. The electron column is shown in Figure 3.7(a) confines the electrons in a particular direction using electric and magnetic fields so that the electron beam hits the desired spot on the surface. These signals may include secondary electron (SE, electrons generated from the sample), backscattered electron (BSE, beam electrons that interact with the atom nuclei and diffract back), X-ray, photons, light, heat, and transmitted electrons. The depth and diameter of electrons penetrating the specimen depend upon the applied voltage and the specimen density. Secondary electrons are collected from the 15-25 nm from the surface, backscattered electrons are collected from the top 40% of the thickness, and x-rays are collected from the entire surface [Reimer, 2000]. A simple SEM image relies on the detection of SE, whereas the BSE and photons are used to understand the crystal structure and the elemental analysis, respectively. The electron beam scans the surface in line by line manner using a set of scan coils. The complete scanning process is conducted under high vacuum conditions to avoid the collision between the electrons and the gas molecules. If in place of a thermionic electron gun, a field emission gun is used, the system is termed as field emission SEM (FESEM) that can produce relatively brighter images due to highly focused electron beam [Egerton, 2005]. Figure. 3.7(a) demonstrates the process of acquiring an SEM image using SE and BSE. Figure 3.7(b) shows the EVO-18 special edition SEM from Carl Zeiss that was used in the

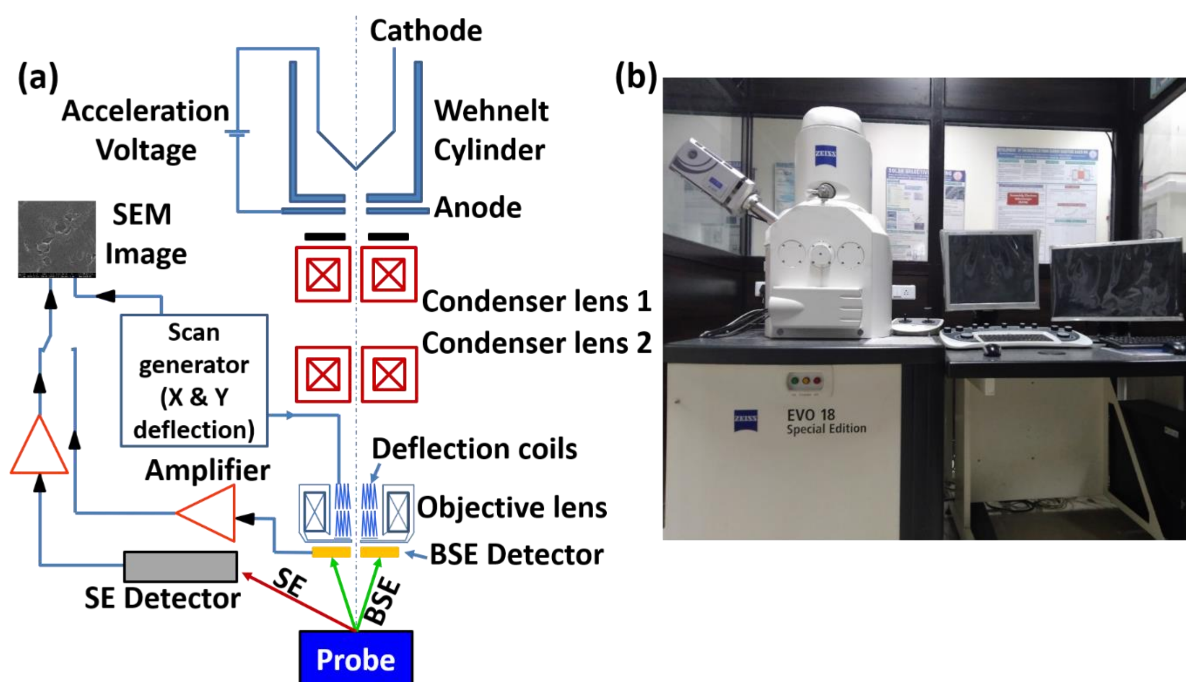

Figure 3.7: (a) Schematic representation of SEM with an electron gun, condenser lens, scanning and deflection coils as the main components. **(b)** EVO-18 special edition SEM from Carl Zeiss used in this research for surface and compositional characterizations.

research. Also, the Nova Nano FESEM 450 (FEI) system was used for topographic and cross-sectional analysis of the films.

3.7 ULTRA-VIOLET AND VISIBLE ABSORPTION SPECTROSCOPY

Ultra-violet and visible spectroscopy (UV-visible spectroscopy) is one of the most popular and useful techniques to understand the chemistry of materials and their nature. This technique analyzes the interaction between the light and the matter in the wavelength range of 200 nm to 800 nm. The energy associated with these rays is high, and their interaction with a molecule causes the transition of an electron from their lower energy levels to the higher [Tomovska *et al.*, 2014]. UV-visible spectroscopy follows the Beer-Lambert law, which states that the absorbance of a solution is directly proportional to the concentration of absorbing material in the solution and the sample length through which light passes [Tomovska *et al.*, 2014]. Thus, for a fixed path length, UV- visible spectroscopy can be used to quantify the concentration of the absorber in the solution. A UV-visible spectrometer consists of a light source that emits radiation in the UV and visible region of the electromagnetic spectrum. The absorption of UV light by the specimen will generate a different spectrum that assists in classify the compound. Moreover, the monochromator selects the wavelength that has to be passed and others will be stopped using diffraction grating or prism. In the current research, the UV-visible spectroscopy analysis was performed in the wavelength range of 200-800 nm [Muñoz Caro, 2018]. Figure 3.8 demonstrates the schematic representation of the UV-visible spectroscopy working principle and inset shows Lambda 750 UV-visible spectrometer by Perkin Elmer used in this research.

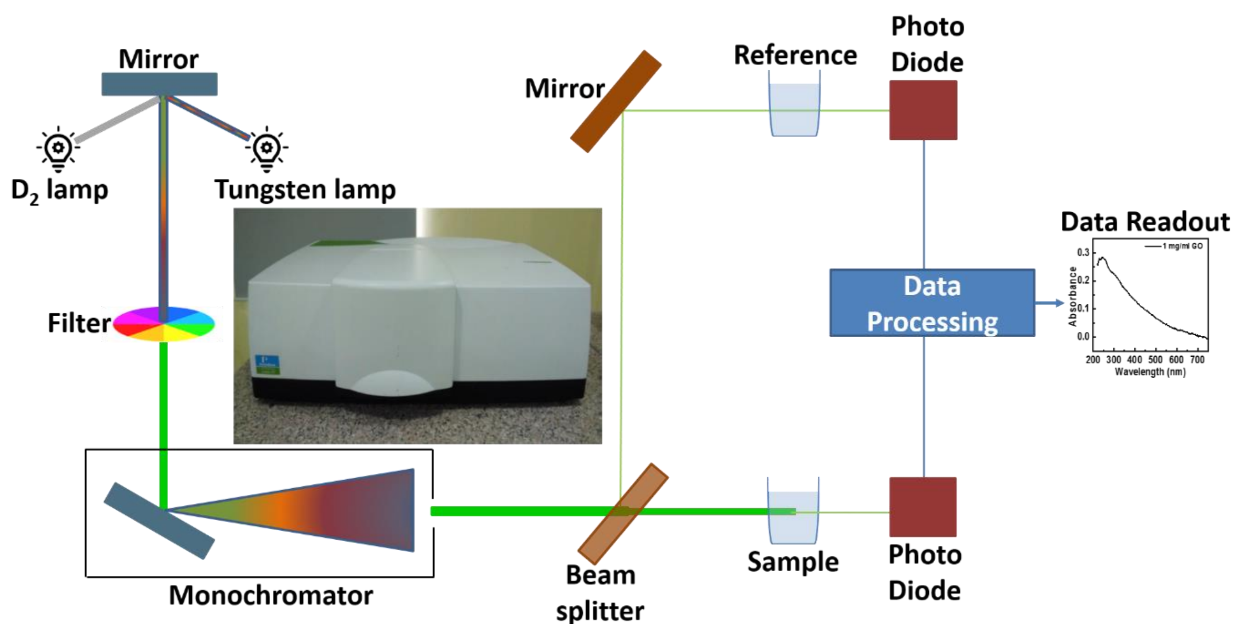

Figure 3.8: (a) Schematic representation of the working principle of UV-visible spectrometer. **(b)** Lambda 750 UV-visible spectrometer by Perkin Elmer used in this characterization. (Image courtesy: http://mrc.mnit.ac.in/#equipments-panel).

3.8 FOURIER-TRANSFORM INFRARED SPECTROSCOPY

The Fourier-Transform infrared spectroscopy (FTIR) is among the oldest and most popular techniques used to identify unknown compounds, additives, and contaminants in any form (solid, liquid, or gas). The basic working of this technique involves calculating the amount of light absorbed by any vibrating molecules when irradiated with infrared (IR) rays that eventually provide a detailed explanation of the molecular fingerprint [Anbusagar *et al.*, 2018]. Several events occur at the molecular level when a molecule absorbs the IR radiations such as

molecular vibrations, bond stretch, and bond bending, resulting from the dipole moment of a molecule. If the natural frequency of vibration of the molecular bond creates a resonance with the IR frequency, the energy will be absorbed, and amplification or attenuation in the energy will be observed [Titus *et al.*, 2019]. This change arises as peaks in the IR spectrum of the specimen. The key components of an FTIR

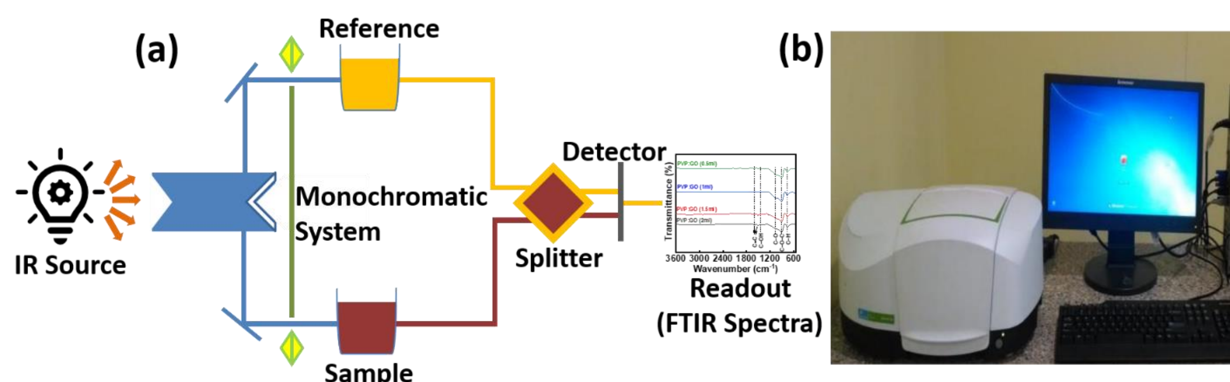

Figure 3.9: (a) Schematic demonstration of FTIR working principle. **(b)** FT-IR Spectrum 2 from Perkin Elmer used in this research. (Image courtesy: http://mrc.mnit.ac.in/#equipments-panel).

instrument are a light source, mirrors, a laser reference, a beam splitter, and a detector. The light interferometer, where it interacts with the beamsplitter that divides it into two beams of same intensity [Berthomieu and Hienerwadel, 2009]. One hits at the fixed mirror that returns back to beamsplitter and other at the moveable source sends the IR radiation into the mirror that makes a pathlength variable with respect to the fixed mirror beam. The two beams generated by the beamsplitter interact with each other to create constructive and destructive interferences called an interferogram. The interferogram is the Intensity Vs. Time spectrum, and when Fourier transform is applied, the Intensity Vs. Frequency spectrum will be obtained that has been used to extract the desired information [Mohamed *et al.*, 2017]. In this research, the FTIR analysis was performed in the range of 3600-600 cm^{-1}. Figure 3.9(a) and (b) display the instrumental schematic of the FTIR system and the digital image of the FT-IR Spectrum 2 from Perkin Elmer system used in this research.

3.9 RAMAN SPECTROSCOPY

Raman spectroscopy is one the most advanced among the spectroscopy techniques for qualitatively and quantitatively analysing the covalently bonded molecules using the vibrational modes associated with them. As the name indicates, the Raman spectroscopy works on the Raman effect, which states that when monochromatic light is incident on a molecule, alteration in the light wavelength will occur, and this alteration will be different for a different molecule [Browne and McGarvey, 2007]. Contrary to the FTIR, Raman spectra can be used to analyse the symmetric molecules such as H_2, N_2, and O_2 using their vibrational levels. Upon the absorption of monochromatic light by a molecule, the light will be scattered in all directions, with some of them having a frequency higher than the incident beam, some have lesser, and some are having the same frequency [Wolverson, 2008]. If the incident and scattered light frequencies are equal, the scattering is termed as the Rayleigh scattering. When the incident light has the frequency higher than the scattered light, the band of frequencies is called the stokes lines on the Rama spectra [Malard *et al.*, 2009]. On the contrary, the band of frequencies with higher frequencies than the incident light is termed as the Antistokes lines. Primary components of a Raman spectrometer consist of sample excitation laser, optical components for sample illumination and light collection, filter for wavelength selector, and charge-coupled device (CCD) detector. After irradiate the device by a Nd:YAG laser, the reflected light is collimated by the lens and directed towards the spectrometer to draw the Raman spectrum [McCreery, 2000]. As Raman is a very

weak effect and it is very difficult to separate the majority of Raman signal i.e. Rayleigh scattering signal. Hence, tuneable and notch filters are fitted into the system to detect the Stokes and Antistokes signals. Figure 3.10(a) and (b) shows the internal architecture of a Raman spectrometer and the digital image**)** STR 500 Raman spectrometer by Airix Corp used in this research.

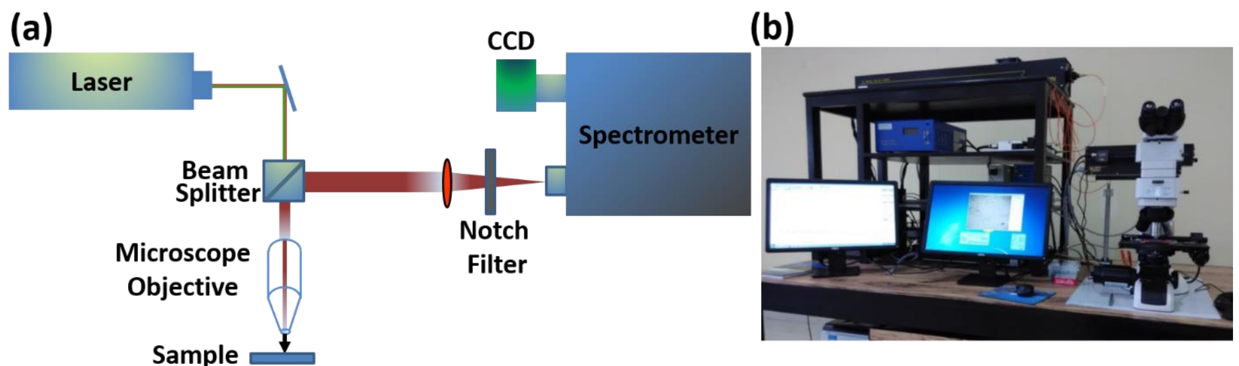

Figure 3.10: (a) Instrumental schematic of Raman spectroscopy. **(b)** STR 500 Raman spectrometer by Airix Corp used in this research. (Image courtesy: http://mrc.mnit.ac.in/#equipments-panel).

3.10 ELECTRICAL CHARACTERIZATION and PARAMETER EXTRACTION

The electrical characterization of the fabricated RRAM devices was performed on Keithley's 4200 Semiconductor Characterization System (SCS) in a custom-designed library for two probe measurements, shown in Figure 3.11(a). The system is capable of characterizing the devices for their current-voltage (*I-V*) and capacitance-voltage (*C-V*) characteristics. The characterization program was executed on the Keithley Interactive Test Environment (KITE) using varying compliance current values, voltage step, and peak voltages in the dual sweep voltage mode. The samples were placed on Cascade Mircotech PM5 probe station with 150 mm chuck mounted over Newport's Benchtop self-levelling pneumatic vibration isolation platform, as displayed in Figure 3.11(b). The device under test was connected to SCS's source measuring units (SMUs) using triax coaxial cables that connect to the probe station.

The choice of a device to be considered for system-level development depends upon various characteristics parameters. The parameters can be related to fabrication processing, fabrication environment, materials, electrical characterization, and chip-level implementation. All these parameters are critical for RRAM performance and device characteristics. The performance of an RRAM device needs to be examined in terms of switching voltage, memory window, reliability, repeatability, sample yield, variability, endurance, retention time, and conduction mechanism [Lanza *et al.*, 2019].

The extraction of the aforementioned parameters requires characterizing the RRAM devices under various test conditions of sweep voltages, voltage bias, voltage pulse, and rising temperature. The initial characteristics were obtained where the applied voltage was plotted with the current on logrithmic scale. These characteristcs demonstrates the resistive switching behavior of the device. A similar curve has been shown in Figure 3.12(a) demonstrating the bipolar resistive switching behavior.

The bias voltage was applied at the top electrode (TE) while the bottom electrode (BE) was kept at the ground potential. The voltage was applied in the sequence of $-V_{stop}\rightarrow 0\rightarrow +V_{stop}\rightarrow 0\rightarrow -V_{stop}$ and the current was measured simultaneously. From $-V_{stop}\rightarrow 0$, the device will remain in its

high resistance state (HRS), and no switching is observed. As the voltage starts increasing on the positive side, the sharp rise in current can be observed at the set voltage (V_{set}), and the device gets switched to a low resistance state (LRS). The primary reason for this transition from HRS to LRS is the migration of metal ions from TE to BE under a high electric field. When the biasing was swept back from $0\rightarrow -V_{stop}$, a sharp drop in the current at reset voltage (V_{reset}) that drives the device back to HRS due to rupture of the conductive region formed between the TE and BE. Moreover, the memory window i.e., I_{on}/I_{off} has been calculated at the read voltage where

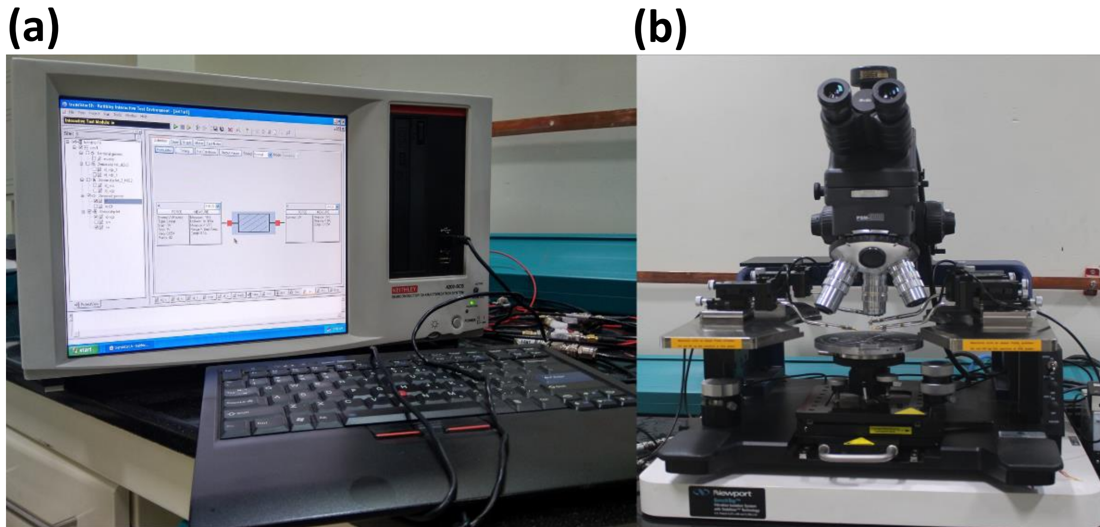

Figure 3.11: (a) 4200-SCS from Keithley used for electrical characterization of RRAM devices. **(b)** PM-5 probe station from Cascade Microtech used for housing and probing sample during electrical characterization.

I_{on}/I_{off} is maximum, and hence device performance doesn't degrade due to external noise or multiple switching events.

The endurance of an RRAM device can be analyzed in two characterization methods. The DC endurance calculation involves the repetition of multiple cycles of switching characteristics, as shown in Figure 3.12(b). However, this method doesn't qualify to calculate the actual

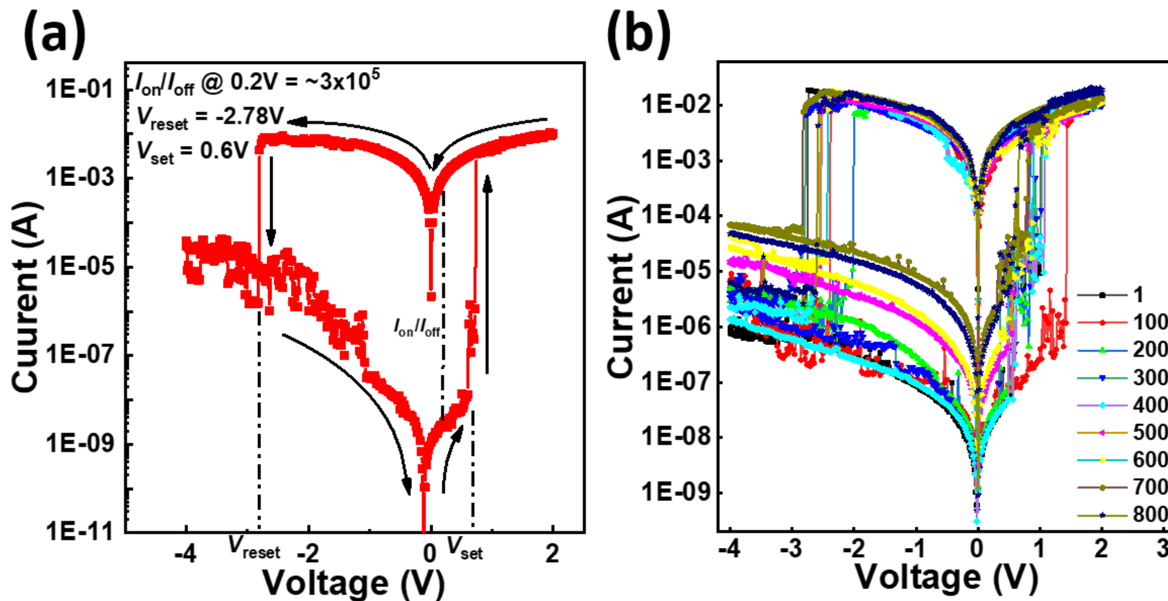

Figure 3.12: (a) Switching characteristics of RRAM device with V_{set} and V_{reset} of 0.6 V and -2.78 V, respectively. **(d)** Shows the DC endurance (repeatability) successfully exhibiting 800 cycles of switching operation.

endurance and the switching speed of the device. Another technique performs the characterization by applying a high-speed square or triangular pulse train of set-read-reset-read sequence, where the current has been read after every transition between the HRS and LRS. An endurance failure will result in either a device couldn't set or reset.

Retention time characteristic is the most important parameter in the case of non-volatile memories. In this research, retention time was calculated by switching the device to that particular state (HRS or LRS) and then applying a voltage bias of 0.2 V read voltage (may vary with device switching characteristics). The retention time points are plotted on logarithmic current against the time. Once the desired retention time of a particular state is recorded, then the

device was switched to the other resistance state, and the same calculations were performed. Finally, both the current values are plotted on a common curve and tested for at least 10 years of retention by extrapolating the time axis. Linear fitting was applied, and the slope of both the state currents was calculated, and then extrapolation gives us an idea of time up to which a sufficient between the two states can be maintained.

Reliability analysis is another important parameter that needs to be examined for the device under test. In this research, the reliability testing has been performed using one of the most popular techniques, the Weibulls distribution that has been plotted for the switching voltage and the current variation in the endurance testing. The switching voltage values have been extracted from each cycle and the arranged in ascending order, and then Weibulls distribution is applied [Varun *et al.*, 2020a]. The Weibulls distribution formula is as following,

$$\ln\text{-}\ln(1\text{-}f(y)) = \beta\ln(x)$$

Where β is the shape factor and also the slope of the distribution curve that has been extracted by applying the linear fit for both the voltages and that decides the reliability of the RRAM device. Higher the β value, the better is the reliability. A similar study has been conducted over the currents in both states plotted for the Weibulls distribution [Chand *et al.*, 2015].